

Scalar fields around a rotating loop quantum gravity black hole: Waveform, quasi-normal modes and superradiance

Zhong-Wu Xia^{1,*}, Hao Yang^{1,†}, and Yan-Gang Miao^{1,2,‡}

¹*School of Physics, Nankai University, Weijin Road 94, Tianjin 300071, China*

²*Faculty of Physics, University of Vienna, Boltzmannngasse 5, A-1090 Vienna, Austria*

Abstract

The rotating loop quantum gravity black hole is a newly proposed non-singular black hole, which eliminates spacetime singularities when a regularization parameter is introduced through loop quantum corrections. This parameter is expected to give rise to observable effects. In this paper, the dynamical behavior of a scalar field near a rotating loop quantum gravity black hole is investigated. Given a small initial perturbation, we obtain the waveform of massless scalar fields evolving over time. By analyzing the waveform, we find that the regularization parameter only affects the damping oscillation of waveform, but not the initial outburst and late-time tail stages. This behavior is characterized by quasi-normal modes. Under scalar field perturbations, the loop quantum black holes remain stable. Moreover, we calculate the quasi-normal modes of massive scalar fields by three numerical methods, which are the Prony, WKB, and shooting methods, respectively. Our results indicate that the real part of quasi-normal modes depends only on the regularization parameter, while the imaginary part does not only on the regularization parameter but also on the angular momentum. Finally, we study the amplification effect of rotating black holes, i.e., the superradiance. Our analyses indicate the existence of stronger superradiance around loop quantum gravity black holes compared to Kerr ones.

*E-mail address: xiazw@mail.nankai.edu.cn

†E-mail address: hyang@mail.nankai.edu.cn

‡Corresponding author. E-mail address: miaoyg@nankai.edu.cn

Contents

1	Introduction	3
2	Rotating black holes in loop quantum gravity	4
3	Time domain waveform	5
3.1	Numerical method	6
3.2	Results	9
4	Quasi-normal modes	9
4.1	Prony method	10
4.2	WKB method	10
4.3	Shooting method	12
4.4	Numerical results	14
4.4.1	Comparison of accuracy among three methods	14
4.4.2	Data of quasi-normal modes	14
5	Superradiance	18
5.1	The Penrose process	19
5.2	Numerical method for superradiance	20
5.3	Results	21
6	Conclusion	21

1 Introduction

Although general relativity (GR) is the most widely accepted theory of gravity, it suffers [1, 2] from several challenges and unresolved issues, such as singularity, information loss paradox, and breakdown of predictability, etc. One effective approach to resolve [3] the conundrum of black hole singularities is to construct regular black hole models. In a regular black hole spacetime, there are no intrinsic singularities, thus naturally avoiding the issues associated with intrinsic singularities. The first regular black hole was constructed [4] within the scope of GR, but latter many regular black holes have been proposed [5–7] in the framework of modified gravity theories. Among the various theories of gravity, the loop quantum gravity (LQG) aims to construct a unified theory of quantum gravity to address the issue of spacetime singularities. Within the scope of LQG theory, some static and spherically symmetric models of regular black holes have been given [8–11], where an extra regularization parameter was introduced.

It is known that astrophysical black holes are rotating, which means that the research on static black holes alone has limited effects on observations. Recently, a rotating model of regular black holes was suggested [12] in the LQG theory, where its shadow was analyzed and connected to possible future observational data [13]. Considering that shadows are only one phenomenon to show the connection between intrinsic properties of black holes and observations, we explore other possible phenomena beyond shadows and investigate their potential observable effects in the scope of LQG theory. In the present work we focus on two phenomena: Quasi-normal modes (QNMs) [14–17] and superradiance [16–18].

Studying perturbations in the background of black holes provides valuable insights into their characteristic signatures, akin to sounds, which can be detected by gravitational wave detectors. Analyzing matter perturbations, such as scalar field perturbations, holds both theoretical significance and observational relevance within the backdrop of black holes. QNMs of a black hole are characteristic oscillations that arise when the black hole is perturbed. In GR, the QNM frequencies of scalar field perturbations are determined by the mass of scalar fields, the mass and angular momentum of black holes. QNMs are complex due to the existence of event horizons, so we can divide a QNM frequency into a real part and an imaginary part,

$$\omega = \omega_{\text{R}} + i\omega_{\text{I}}, \quad (1)$$

where the real part ω_{R} represents the oscillation frequency and the imaginary part ω_{I} denotes the decay rate. In previous works [14], it has been noted that QNMs are highly sensitive to boundary conditions, particularly the asymptotic behaviors of scalar fields near event horizons. The difference between a LQG metric and a Kerr metric will lead to differences of boundary conditions and then affect QNMs. In astrophysical observations the ringdown phase after the merger of two black holes is described by perturbation theory and gravitational waves are a linear superposition of QNMs [19–21]. Through computing the QNMs of scalar field perturbations around a rotating LQG black hole (rLQGBH), we can provide some hints of the underlying gravity theory.

The superradiance effect is a radiation enhancement process in a dissipative system, such as a near-extreme black hole. In black hole theory, the superradiance is closely associated [22–25] with the ergoregion of rotating black holes. Especially, the superradiance is a powerful tool to detect [18, 26] ultralight scalar fields which are a promising candidate of dark matter. Similar to QNMs, the superradiance is also

sensitive to boundary conditions, thus the regularization parameter will leave imprints on the superradiance effects in rLQGBHs, too. We expect to shed some light on the existence of ultralight scalar particles in the LQG theory through the investigation of superradiance.

Our research focuses on QNMs and superradiance effects, both of which need to deal with Klein-Gordon equations with boundary conditions. The difficulty of calculations lies in the complicity of rLQGBHs, where one aspect comes from the angular equation due to rotations, and the other comes from the complicated radial equation. Although it has widely been applied in GR, see, for instance, Refs. [27, 28], the Leaver method is unable to deal with rLQGBHs because a five-term recurrence relation, rather than a three-term one, appears in solving the radial equation of rLQGBHs. Owing to this reason, we employ three other numerical methods, the Prony, WKB, and shooting methods, to calculate the QNMs of scalar field perturbations around rLQGBHs and compare the results among the three methods in order to obtain the most precise QNMs. Moreover, we analyze the superradiance effect in rLQGBHs by adopting the shooting method which is the most efficient one among the three.

The paper is organized as follows. In Sec. 2, we briefly introduce the rotating black holes in loop quantum gravity. In Sec. 3, we analyze the time domain waveform under scalar field perturbations. In Sec. 4, we compute the QNMs of scalar field perturbations around rLQGBHs by using the three numerical methods. In Sec. 5, we apply the shooting method to calculate the amplification factor. Finally, we give our conclusion in Sec. 6. The natural units ($G = c = \hbar = 1$) are adopted in our paper.

2 Rotating black holes in loop quantum gravity

In this section we briefly describe the geometry of rLQGBHs. From a static and spherically symmetric LQGBH, its rotating counterpart was constructed [12, 29] in terms of the modified Newman-Janis algorithm. In the Boyer-Lindquist coordinates (t, r, θ, φ) , the line element of rLQGBHs reads

$$ds^2 = - \left(1 - \frac{2Mb}{\rho^2} \right) dt^2 - \frac{4aMb \sin^2 \theta}{\rho^2} dt d\varphi + \rho^2 d\theta^2 + \frac{\rho^2}{\Delta} dr^2 + \frac{\Sigma \sin^2 \theta}{\rho^2} d\varphi^2, \quad (2)$$

where the relevant quantities are defined by

$$\rho^2 = a^2 \cos^2 \theta + b^2, \quad (3)$$

$$\Delta = b^2 + a^2 - 2Mb, \quad (4)$$

$$\Sigma = (b^2 + a^2)^2 - a^2 \Delta \sin^2 \theta, \quad (5)$$

$$b^2 = \frac{A_\lambda}{\sqrt{1+x^2}} \frac{M_B^2 (x + \sqrt{1+x^2})^6 + M_B^2}{(x + \sqrt{1+x^2})^3}, \quad (6)$$

$$M = \frac{b}{2} \left[1 - \frac{8A_\lambda M_B^2}{b^2} \left(1 - \sqrt{\frac{1}{2A_\lambda} \frac{1}{\sqrt{1+x^2}}} \right) (1+x^2) \right], \quad (7)$$

$$x = \frac{r}{\sqrt{8A_\lambda M_B}}. \quad (8)$$

Here the angular momentum a and Arnowitt-Deser-Misner (ADM) mass M_B are assumed to be positive, and A_λ is a positive dimensionless parameter, here called regularization parameter, which originated [10] from quantum modifications. The above rLQGBH is regular [12] everywhere when $A_\lambda > 0$ and reduces to a Kerr black hole when $A_\lambda = 0$. By introducing a coordinate transformation,

$$h = \sqrt{r^2 + 8A_\lambda M_B^2}, \quad (9)$$

we rewrite ρ^2 , Δ , Σ , b^2 , and M to be

$$\rho^2 = a^2 \cos^2 \theta + h^2 - 6A_\lambda M_B^2 \quad (10)$$

$$\Delta = h^2 + a^2 - 2M_B h, \quad (11)$$

$$\Sigma = (h^2 - 6A_\lambda M_B^2 + a^2)^2 - a^2 \Delta \sin^2 \theta, \quad (12)$$

$$b^2 = h^2 - 6A_\lambda M_B^2, \quad (13)$$

$$M = \frac{M_B h - 3A_\lambda M_B^2}{b}. \quad (14)$$

The location of horizons can be determined by the algebraic equation, $\Delta = 0$, and its solutions are

$$h_{\pm} = M_B \pm \sqrt{M_B^2 - a^2}, \quad (15)$$

where a plus or minus sign represents an outer or inner horizon. According to the existence of an outer horizon, we restrict the two dimensionless parameters, A_λ and a/M_B in the shadow region of Fig. 1, where the blue curve corresponds to the extreme configuration. From the parameter space $(A_\lambda, a/M_B)$, we obtain that the maximum value of angular momenta equals to the ADM mass, $a_{\text{Max}}/M_B = 1$, which will be adopted in the numerical calculations below. For a given angular momentum a , the entire range of regularization parameter A_λ is $0 \leq A_\lambda \leq A_{\lambda\text{Max}}$, where the extreme configuration of rLQGBHs takes the maximum value of A_λ ,

$$A_{\lambda\text{Max}} = \frac{1}{8} \left(1 + \sqrt{1 - \frac{a^2}{M_B^2}} \right)^2. \quad (16)$$

3 Time domain waveform

Theoretical studies have shown that the temporal evolution of perturbations in the presence of black holes typically undergoes [14] three distinct stages. Following the initial pulse, the perturbation field enters a phase of damping oscillations known as quasi-normal ringing, characterized by frequencies and damping times, i.e. QNMs, solely determined by the black hole parameters. At the last stage of late-time tails, the damping oscillations are overwhelmed by a relaxation process.

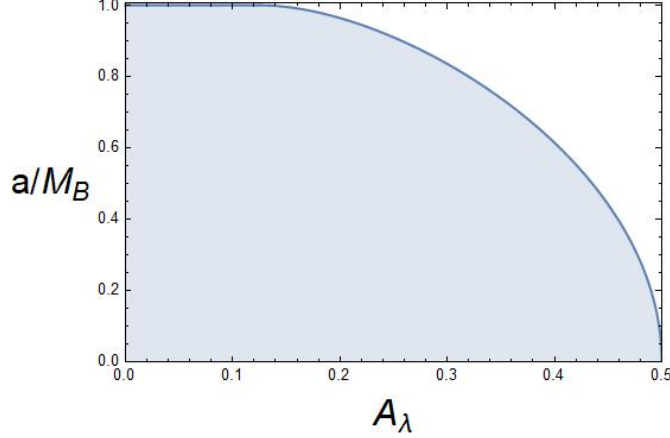


Figure 1: The parameter space $(A_\lambda, a/M_B)$ of rLQGBH spacetime, where the shadow region is allowed.

3.1 Numerical method

For a massless scalar perturbation around an rLQGBH, the equation of motion is the massless Klein-Gordon equation,

$$\nabla^\nu \nabla_\nu \Phi = 0, \quad (17)$$

where Φ is the wave function. Generally, we can simulate the waveform Φ of scalar fields by solving the above equation in (t, r, θ, φ) coordinates. In the Boyer-Lindquist coordinate system, the radial range is taken to be $(h_+, +\infty)$ in computation. Traditionally, this range is mapped into $(-\infty, +\infty)$ by the tortoise coordinate system. However, it is impossible to perform a numerical integration over a range that extends to $(-\infty, +\infty)$ in practice. Thus, a truncation near the event horizon and infinity is necessary to render the range finite. Unfortunately, such a truncation introduces [30, 31] artificial boundaries to scalar fields, leading to spurious wave reflections that can spoil the late-time tail of scalar field evolution. To address the boundary issue inherent in the traditional foliation, a horizon-penetrating hyperbolic (HH) foliation is designed.

In the first transformation, we construct the horizon-penetrating coordinates $\{\tilde{t}, h, \theta, \tilde{\varphi}\}$ through

$$d\tilde{t} = dt + \frac{2Mb}{\varepsilon\Delta} dh, \quad d\tilde{\varphi} = d\varphi + \frac{a}{\varepsilon\Delta} dh, \quad (18)$$

where ε is defined by

$$\varepsilon = \sqrt{1 - \frac{8A_\lambda M_B^2}{h^2}}. \quad (19)$$

The rLQGBH metric Eq. (2) then becomes

$$\begin{aligned} ds^2 = & - \left(1 - \frac{2Mb}{\rho^2}\right) d\tilde{t}^2 - \frac{4aMb}{\rho^2} \sin^2\theta d\tilde{t}d\tilde{\varphi} + \frac{4Mb}{\varepsilon\rho^2} d\tilde{t}dh \\ & + \frac{1}{\varepsilon^2} \left(1 + \frac{2Mb}{\rho^2}\right) dh^2 - \frac{2}{\varepsilon} a \sin^2\theta \left(1 + \frac{2Mb}{\rho^2}\right) dh d\tilde{\varphi} \\ & + \rho^2 d\theta^2 + \left(b^2 + a^2 + \frac{2Mba^2 \sin^2\theta}{\rho^2}\right) \sin^2\theta d\tilde{\varphi}^2. \end{aligned} \quad (20)$$

Since the metric does not contain $\tilde{\varphi}$ explicitly, $\partial_{\tilde{\varphi}}$ is Killing vector. Therefore, we can separate variable $\tilde{\varphi}$ from the scalar field function,

$$\Phi(\tilde{t}, h, \theta, \tilde{\varphi}) = \frac{1}{h} \sum_m \psi(\tilde{t}, h, \theta) e^{im\tilde{\varphi}}, \quad (21)$$

where m is azimuthal number. After substituting the above expression into Eq. (17), we can express the Klein-Gordon equation as

$$A^{\tilde{t}\tilde{t}} \partial_{\tilde{t}}^2 \psi + A^{\tilde{t}h} \partial_{\tilde{t}} \partial_h \psi + A^{hh} \partial_h^2 \psi + A^{\theta\theta} \partial_\theta^2 \psi + B^{\tilde{t}} \partial_{\tilde{t}} \psi + B^h \partial_h \psi + B^\theta \partial_\theta \psi + C \psi = 0, \quad (22)$$

where the coefficient functions take the forms,

$$\begin{aligned} A^{\tilde{t}\tilde{t}} &= \rho^2 + 2Mb, \\ A^{\tilde{t}h} &= -4\epsilon Mb, \\ A^{hh} &= -\epsilon^2 \Delta, \\ A^{\theta\theta} &= -1, \\ B^{\tilde{t}} &= 2M_B \epsilon - \epsilon \frac{12A_\lambda M_B^2}{h}, \\ B^h &= \epsilon^2 \frac{2}{h} (a^2 - M_B h) - 2ima\epsilon - \epsilon \Delta \frac{d}{dh} \epsilon, \\ B^\theta &= -\cot\theta, \\ C &= \frac{m^2}{\sin^2\theta} - \epsilon^2 \frac{2(a^2 - M_B h)}{h^2} + \epsilon \frac{2ima}{h} + \epsilon \frac{\Delta}{h} \frac{d}{dh} \epsilon. \end{aligned} \quad (23)$$

In the second transformation, we introduce the hyperbolic foliation [32] to define the compact horizon-penetrating and hyperboloidal coordinates (HH coordinates), $\{\tau, \tilde{r}, \theta, \tilde{\varphi}\}$,

$$\tilde{t} = \tau + f(\tilde{r}), \quad h = \frac{\tilde{r}}{\Omega(\tilde{r})}, \quad (24)$$

where

$$f(\tilde{r}) = \frac{\tilde{r}}{\Omega(\tilde{r})} - \tilde{r} - 4M_B \ln \Omega(\tilde{r}), \quad \Omega(\tilde{r}) = 1 - \frac{\tilde{r}}{S}. \quad (25)$$

Here S is a constant associated with the hyperbolic foliation. According to this coordinate transformation and Eq. (15), we obtain the location of the outer horizon,

$$\tilde{r}_+ = \frac{a^2 S + \left(M_B + \sqrt{M_B^2 - a^2} \right) S^2}{a^2 + 2M_B S + S^2}, \quad (26)$$

and the relations between the HH coordinates and the horizon-penetrating coordinates,

$$\partial_{\tilde{t}} = \partial_\tau, \quad \partial_h = -H \partial_\tau + K \partial_{\tilde{r}}, \quad (27)$$

where

$$H = \frac{df(\tilde{r})}{dh}, \quad K = \frac{d\tilde{r}}{dh}. \quad (28)$$

Therefore, the Klein-Gordon equation Eq. (22) can be expressed in the HH coordinates as follows:

$$\partial_\tau^2 \psi = \tilde{A}^{\tau\tilde{r}} \partial_\tau \partial_{\tilde{r}} \psi + \tilde{A}^{\tilde{r}\tilde{r}} \partial_{\tilde{r}}^2 \psi + \tilde{A}^{\theta\theta} \partial_\theta^2 \psi + \tilde{B}^\tau \partial_\tau \psi + \tilde{B}^{\tilde{r}} \partial_{\tilde{r}} \psi + \tilde{B}^\theta \partial_\theta \psi + \tilde{C} \psi, \quad (29)$$

where the new coefficient functions have the following connections to the previous ones given by Eq. (23),

$$\begin{aligned} \{\tilde{A}^{\tau\tilde{r}}, \tilde{A}^{\tilde{r}\tilde{r}}, \tilde{A}^{\theta\theta}, \tilde{B}^\tau, \tilde{B}^{\tilde{r}}, \tilde{B}^\theta, \tilde{C}\} &= -\frac{1}{A^{\tau\tau}} \{A^{\tau\tilde{r}}, A^{\tilde{r}\tilde{r}}, A^{\theta\theta}, B^\tau, B^{\tilde{r}}, B^\theta, C\}, \\ A^{\tau\tau} &= A^{\tilde{r}\tilde{r}} - HA^{\tilde{r}h} + H^2 A^{hh}, \\ A^{\tau\tilde{r}} &= KA^{\tilde{r}h} - 2KHA^{hh}, \\ A^{\tilde{r}\tilde{r}} &= K^2 A^{hh}, \\ B^\tau &= B^{\tilde{r}} - HB^h - \frac{dH}{d\tilde{r}} KA^{hh}, \\ B^{\tilde{r}} &= K \left(B^h + \frac{dK}{d\tilde{r}} A^{hh} \right). \end{aligned} \quad (30)$$

After the above two coordinate transformations, the radial coordinate is mapped to $\tilde{r} \in [\tilde{r}_+, S)$, where \tilde{r}_+ is defined by Eq. (26) and S is an arbitrarily chosen positive constant larger than \tilde{r}_+ . When executing the numerical calculation, the integration is only performed within the computational region, $\tilde{r} \in [\tilde{r}_+, S)$. For the other regions, $\tilde{r} \notin [\tilde{r}_+, S)$, the wave function is set to zero. This mapping confines the range of the radial coordinate to a finite interval, thus naturally imposing boundary conditions without the need for manual specification at the two endpoints. This technique ensures that the scalar field at any moment is only related to itself from the previous moment in $\tilde{r} \in [\tilde{r}_+, S)$, and unrelated to the other regions. Such a treatment is equivalent to the boundary conditions with only incoming waves at the event horizon and outgoing waves at the null infinity, naturally coinciding with the boundary conditions for QNMs. And it simplifies the computational region and avoids the introduction of artificial boundary effects that could affect the accuracy of simulation results for the scalar field's evolution. Therefore, the HH coordinate system does not require any truncation to perform the numerical integration. In order to numerically solve Eq. (29), we introduce an auxiliary function Π , so that we can reduce this equation to two first-order equations,

$$\partial_\tau \psi = \Pi, \quad (31)$$

$$\partial_\tau \Pi = \tilde{B}^\tau \Pi + \tilde{A}^{\tau\tilde{r}} \partial_{\tilde{r}} \Pi + \tilde{A}^{\tilde{r}\tilde{r}} \partial_{\tilde{r}}^2 \psi + \tilde{A}^{\theta\theta} \partial_\theta^2 \psi + \tilde{B}^{\tilde{r}} \partial_{\tilde{r}} \psi + \tilde{B}^\theta \partial_\theta \psi + \tilde{C} \psi, \quad (32)$$

which can be solved by the fourth-order Runge-Kutta method [33]. Here we take a Gaussian wave packet as the initial condition,

$$\begin{aligned} \psi(\tau = 0, \tilde{r}, \theta) &= Y_{lm}(\theta) \exp \left[-\frac{(\tilde{r} - \tilde{r}_c)^2}{2\sigma^2} \right], \\ \Pi(\tau = 0, \tilde{r}, \theta) &= 0, \end{aligned} \quad (33)$$

where $Y_{lm}(\theta)$ is the θ -dependent part of spherical harmonics, and \tilde{r}_c and σ are the center and width of Gaussian packets, respectively. We choose the location of our observer to be $\tilde{r}_c = 6M_B$, $\theta = \frac{\pi}{4}$, the width of wave packets to be $\sigma = 0.2$, and the free parameter to be $S = 10$ as suggested by Refs. [31, 32], then we solve Eqs. (31) and (32) and obtain the time domain evolution profiles.

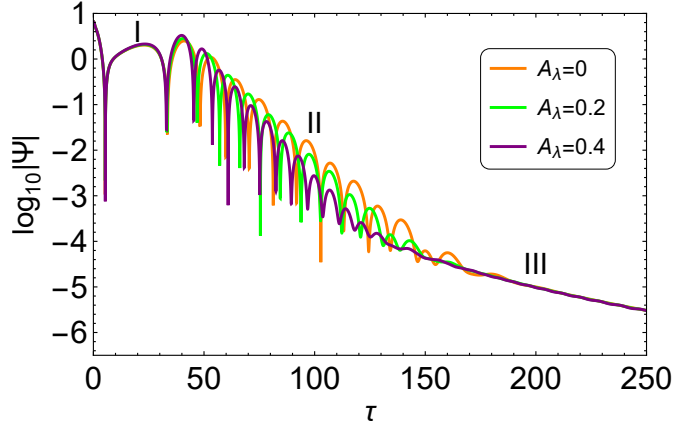


Figure 2: The waveform of massless scalar perturbations with various values of A_λ , where the initial mode is chosen to be $l = 1 = m$, and $M_B = 1$ and $a = 0.1$ are set. Three distinct phases are notable, where phase I is initial outburst, phase II damping oscillation, and phase III late-time tail.

3.2 Results

We choose $l = 1 = m$ as our initial mode and draw the waveform of a massless scalar field perturbation around an rLQGBH in Fig. 2. Analyzing the evolution profiles, we observe that the introduction of regularization parameter A_λ does not significantly affect the evolution of outbursts and late-time tails. However, it exerts a notable influence on the damping oscillation phase, that is, an increase of A_λ leads to an accelerated oscillation and a rapider decay of scalar fields. Therefore, in order to distinguish LQG from GR, i.e., an rLQGBH from a Kerr black hole, we need to study the QNM frequencies of the damping oscillation stage. In the subsequent section, we provide a detailed investigation on the influence of A_λ on the QNMs under scalar field perturbations.

4 Quasi-normal modes

If a scalar field meets the specific boundary conditions:¹ Pure ingoing waves exist at the outer horizon of black holes, while pure outgoing waves exist at the spatial infinity, the characteristic complex frequencies of damping oscillations are just QNMs. Owing to the complicated boundary conditions around rLQGBHs, it is not feasible to obtain QNMs precisely through analytical methods. As a result, various numerical and semi-analytical methods have been adopted [14–17, 35–39]. Each method possesses its own advantages and disadvantages, so that the accuracy of results cannot be guaranteed if one relies solely on a single method. In this section, we employ three methods to compute QNMs and make comparisons among them in order to ensure the accuracy and reliability of our findings.

As shown in Ref. [31], the choice of coordinate systems mainly affects the late-time tail stage of scalar field evolution but hardly the second phase, the damping oscillation stage. Since QNMs are char-

¹Such boundary conditions always hold for any asymptotically flat spacetime, such as the rLQGBHs we are considering. However, for any asymptotic AdS spacetime, there exist other boundary conditions and corresponding QNMs, see for instance, one of our recent papers [34].

acteristic frequencies of the damping oscillation stage, both the conventional and horizon-penetrating hyperbolic coordinate systems are suitable. Considering that the radial equation in the former system is much simpler than that in the latter one, we choose the former coordinate system when computing QNMs.

4.1 Prony method

In Sec. 3 we have presented the approach for obtaining time domain profiles of massless scalar field perturbations in rLQGBHs. Now we can extract QNMs from these profiles by the Prony method [14, 35]. The main idea of this method is to fit the profile data with a superposition of damping exponents,

$$\Phi(t) \sim \sum_{j=1}^p C_j e^{-i\omega_j t}, \quad (34)$$

where C_j is the amplitude coefficient of QNMs. In computations, we extract $(2p - 1)$ equidistant points from the damping oscillation phase of a profile. These points are used to form one $p \times p$ matrix in order to calculate ω_j . Here rows and columns of this metric are composed of equidistant points with decreasing sequence numbers. Among the p ω_j 's, the one with the largest $|C_j|$ is dominant, which is our demanding QNM frequency.

Although the QNMs obtained through the Prony method exhibit [31] a high precision, our (2+1)-dimensional simulation approach cannot capture the waveform of massive scalar fields, making the QNMs of massive scalar field perturbations unavailable. Therefore, alternative methods must be employed to compute the QNMs for massive scalar field perturbations in the subsequent sections.

4.2 WKB method

The WKB method is a semi-analytic technique for determining low-lying QNMs [39]. For a massive scalar perturbation around an rLQGBH, the massive Klein-Gordon equation is

$$\nabla^\nu \nabla_\nu \Phi = \mu^2 \Phi, \quad (35)$$

where μ is the mass of scalar fields. Assuming that a scalar field has the same symmetry as that of its background spacetime, we can make the following ansatz,

$$\Phi(t, h, \theta, \varphi) = \int e^{-i\omega t} \sum_{l,m} S_{lm}(\theta) R_{lm}(h) e^{im\varphi} d\omega, \quad (36)$$

where h is defined by Eq. (9), l stands for the angular momentum number, and ω denotes the characteristic frequency of scalar fields. After separating variables, we obtain the angular equation,

$$\frac{1}{\sin\theta} \frac{d}{d\theta} \left[\sin\theta \frac{d}{d\theta} S_{lm}(\theta) \right] + \left[a^2 (\omega^2 - \mu^2) \cos^2\theta - \frac{m^2}{\sin^2\theta} + A_{lm} \right] S_{lm}(\theta) = 0, \quad (37)$$

where $S_{lm}(\theta)$ is spherical harmonics [17], which reduces to $Y_{lm}(\theta)$ when $a^2(\omega^2 - \mu^2)\cos^2\theta = 0$, and A_{lm} is angular eigenvalue. The radial equation reads

$$\varepsilon \frac{d}{dh} \left[\varepsilon \Delta \frac{d}{dh} R_{lm}(h) \right] + \left[\frac{\tilde{K}^2}{\Delta} - \mu^2 b^2 - (A_{lm} - 2am\omega + a^2\omega^2) \right] R_{lm}(h) = 0, \quad (38)$$

where $\tilde{K} = am - (b^2 + a^2)\omega$. By introducing the following transformation,

$$\Psi(y) = (b^2 + a^2)^{1/2} R_{lm}(h), \quad (39)$$

we can change the radial equation of motion to a Schrödinger-like one,

$$\frac{d^2}{dy^2} \Psi(y) + [\omega^2 - V(y, \omega)] \Psi(y) = 0, \quad (40)$$

where y is the tortoise coordinate determined by

$$\frac{dh}{dy} = \frac{\varepsilon \Delta}{b^2 + a^2}, \quad (41)$$

and $V(y, \omega)$ is the effective potential,

$$\begin{aligned} V(y, \omega) &= V_1 + V_2, \\ V_1 &= \frac{\Delta}{h(b^2 + a^2)^4} \left\{ -96A_\lambda^2 M_B^4 (M_B - h) + a^4 h + 2M_B h^4 \right. \\ &\quad \left. - 2A_\lambda M_B^2 h^2 (4M_B + 5h) + a^2 [h^2 (-4M_B + h) + 2A_\lambda M_B^2 (8M_B + h)] \right\}, \\ V_2 &= \frac{\Delta}{(b^2 + a^2)^2} \left[\frac{\tilde{K}^2}{\Delta} - \mu^2 b^2 - (A_{lm} - 2am\omega + a^2\omega^2) \right]. \end{aligned} \quad (42)$$

According to Refs. [17, 40], we find that the fourth-order WKB approximation is the most suitable for the case of rotating black holes among all orders' WKB approximations. Therefore, we choose the fourth-order WKB approximation to numerically solve the radial equation. Despite its minimal computational resource requirement, the fourth-order WKB approximation exhibits a very small error compared to the more precise sixth-order WKB approximation. The QNM frequency ω is given by the WKB formula [38, 41]:

$$\frac{i[\omega^2 - V(y_0, \omega)]}{\sqrt{-2V''(y_0, \omega)}} - \sum_{j=2}^4 \Lambda_j = n + \frac{1}{2}, \quad n = 0, 1, 2, \dots, \quad (43)$$

where the prime means the derivative with respect to the tortoise coordinate, and y_0 is fixed by the condition,

$$\frac{d}{dy} V(y, \omega) \Big|_{y=y_0} = 0, \quad (44)$$

and Λ_j denotes higher order correction terms. The specific form of Λ_j is given in Ref. [41].

Rotating black holes are more intricate than static ones because both the scalar potential $V(y, \omega)$ and the angular eigenvalue A_{lm} depend on the frequency ω in the case of rotating black holes. For massless

scalar field perturbations, we utilize [39] the series expansion method to solve Eq. (43), retaining the terms up to $(a\omega)^6$. However, for massive scalar field perturbations, the angular eigenvalue A_{lm} should be expanded as a series of $(a\sqrt{\omega^2 - \mu^2})$ because only even-order terms appear due to the absence of spin for scalar particles. The expansion takes the form:

$$A_{lm} = {}_0f_0^{lm} + {}_0f_2^{lm} a^2 (\omega^2 - \mu^2) + {}_0f_4^{lm} a^4 (\omega^2 - \mu^2)^2 + \dots, \quad (45)$$

and ${}_0f_j^{lm}$ is the j th order expansion coefficient. By employing the expressions of A_{lm} and y_0 , we can also express both V_0 and its higher order derivatives as series of $(a\omega)$ up to order $(a\omega)^6$. Finally, we solve Eq. (43) numerically and determine the QNMs with the fixed values of a , μ , n , l , and m .

The advantage of the WKB method lies in its polynomial formula with which we can obtain QNMs with high accuracy through simple numerical calculations. As discussed above, this method depends only on the first six terms of series expansions. However, these terms diverge in certain cases, which leads to a breakdown of the method. The applicable condition can be given in a specific range of parameter a . In calculations we cannot directly apply the WKB formula to rotating black holes because the radial potential $V(y, \omega)$ in Eq. (40) involves an unknown frequency. Instead, we seek help from the series expansion. When requiring the convergence of this series, we obtain the applicable condition under an appropriate approximation. For the detailed discussions, see Sec. 4.4.1, where the WKB method is extrapolated to be valid in the range of $a \lesssim 0.4$.

4.3 Shooting method

The shooting method is a straightforward numerical strategy [17, 36] for solving ordinary differential equation and determining QNMs. The key issue to obtain QNMs is the precise numerical integration of the radial equation of motion. This process initiates from a proximal vicinity of the event horizon and extends toward an arbitrarily selected intermediate point. Conversely, a similar integration procedure is conducted from a position near the spatial infinity back to the same intermediate locale. The crux of the method hinges upon ensuring continuity and differentiability of the wave functions across this junction, that is, both the wave functions and their first-order derivatives, as calculated from the aforementioned disparate starting points, must converge and exhibit equality at the intermediate point. This condition ensures the physical validity and continuity of the solution in the domain from the event horizon to infinity, reflecting the underlying physics of black hole perturbations and the propagation of waves in their vicinity.

To fulfill our objectives, we conduct a comprehensive analysis of the asymptotic behaviors associated with the radial equation as delineated in Eq. (38). Notably, the outer event horizon, denoted as $h = h_+$, and the spatial infinity, represented by $h = h_\infty$, constitute two regular singular points for the radial equation. Consequently, it becomes feasible to represent the radial wave function $R(h)$ through two convergent series near the two boundaries.

Near the outer event horizon, the radial wave function $R(h)$ has the following asymptotic behavior,

$$R(h) \sim (h - h_+)^{\pm i\alpha}, \quad (46)$$

where α is a parameter to be fixed and h_+ and h_- are determined by Eq. (15) for rLQGBHs. Then we substitute Eq. (46) into Eq. (38) and solve it. Thus, we derive the specific form of α ,

$$\alpha = \frac{am - 2M_B \omega(h_+ - 3A_\lambda M_B)}{\varepsilon_+(h_+ - h_-)}, \quad \varepsilon_+ = \sqrt{1 - \frac{8A_\lambda M_B^2}{h_+^2}}. \quad (47)$$

Near the spatial infinity, we perform an asymptotic expansion of Eq. (38) and find that $R(h)$ takes the form,

$$R(h) \sim \frac{1}{h} e^{\pm qh} h^{\pm M_B(\mu^2 - 2\omega^2)/q}, \quad q = \sqrt{\mu^2 - \omega^2}. \quad (48)$$

In Eq. (46) the plus and minus signs correspond to ingoing and outgoing waves, respectively. In contrast, the plus and minus signs correspond to outgoing and ingoing waves in Eq. (48), respectively.

QNMs are characterized as the eigenvalues of wave equations that adhere to stringent boundary conditions, stipulating the exclusive presence of ingoing waves in the vicinity of event horizons and solely outgoing waves at the spatial infinity. These boundary conditions profoundly influences the selection of suitable asymptotic behaviors for the wave function $R(h)$. Consequently, for an accurate representation of the wave dynamics near these critical regions, we adopt the following asymptotic expressions: Near the outer event horizon, the radial wave function $R(h)$ asymptotically approaches:

$$R(h) \sim (h - h_+)^{i\alpha}, \quad (49)$$

and near the spatial infinity, the asymptotic behavior takes the form:

$$R(h) \sim \frac{1}{h} e^{qh} h^{M_B(\mu^2 - 2\omega^2)/q}. \quad (50)$$

Utilizing the shooting method, we can now accurately compute the QNMs in the range of $h_+ < h < h_\infty$. Initially, we select a preliminary QNM frequency to serve as our initial guess. With this frequency we can determine the angular eigenvalue A_{lm} by the Leaver method [27]. Subsequently, in alignment with the asymptotic behavior delineated by Eq. (49) in the proximity of the outer event horizon, we numerically integrate Eq. (38), commencing from the outer event horizon to a strategically chosen intermediate location. This point is typically selected to coincide with the peak of the potential function, optimizing the accuracy of our integration process. In the ensuing phase, considering the asymptotic behavior presented in Eq. (50) near the spatial infinity, we integrate Eq. (38) from infinity back to the aforementioned intermediate point. The last step is to ensure the continuity for both the radial wave function $R(h)$ and its first derivative $R'(h)$ at the intermediate junction. Achieving this continuity allows us to ascertain a QNM frequency. This newly determined QNM frequency is then employed as the initial value for the subsequent iteration. Through this iterative refinement, we ultimately converge upon a stable QNM frequency, thus fulfilling our objective of accurately determining the QNMs.

The shooting method stands out for its exceptional stability, enabling it to handle the situations in which the Prony method and WKB method fail. However, the outcomes of the shooting method are highly dependent on the selection of initial values. In calculations, the initial values of QNMs are typically determined [27] by the QNMs of Kerr black holes. With the above setup, we are able to compute QNMs through the shooting method.

4.4 Numerical results

4.4.1 Comparison of accuracy among three methods

Utilizing the three methodologies described, we successfully compute the QNMs for scalar field perturbations in the background of rLQGBHs. We commence our discussion by showcasing the QNMs of massless scalar field perturbations, which vary with the regularization parameter A_λ , as delineated in Tab. 1. Specifically, we examine two modes, namely $l = 1 = m$ and $l = 2 = m$. In the notable instance with $A_\lambda = 0$, an rLQGBH simplifies to a Kerr black hole. It is noteworthy that our results align with those obtained [42] via the Leaver method for Kerr black holes, thereby underscoring the accuracy and reliability of our analysis.

Since the Prony method is completely a numerical calculation of waveform simulations, its accuracy and reliability are the highest among the three methods, so we take its results as the standard to measure the accuracy of the results from the other two methods. Here, we define the relative error between data D and standard data SD as follows:

$$\text{Err} = \left| \frac{D - SD}{D} \right|, \quad (51)$$

and display the relative errors between the QNMs obtained by the Prony method and those by the other two methods in the brackets of Tab. 1, where the left of brackets shows the relative error of real parts, while the right that of imaginary parts. We can see that the relative errors are almost all less than 2%, indicating that both the WKB method and shooting method exhibit high accuracy within the range of regularization parameter A_λ , $0 \leq A_\lambda \leq 0.45$. However, in the mode of $l = 1 = m$, the relative errors associated with the WKB method grow with an increase of regularization parameter A_λ , which implies that this method may not work well when other parameters, such as angular momenta, take a certain range.

In order to further study the scope of application of the WKB method and the impact of angular momentum a on the QNMs of massless (*massive*) scalar field perturbations, we display in Tab. 2 the relationship between the QNMs and a , where $A_\lambda = 0.1$ and $l = 1 = m$ are set. When $a \lesssim 0.4$, the QNMs obtained from the three (*two*) methods are consistent. However, if $a \gtrsim 0.4$, the discrepancy between the WKB method and the other two methods (*shooting method*) rapidly increases. The reason is that the series of $(a\omega)$ no longer converges in the WKB method if $a \gtrsim 0.4$, rendering the WKB method inapplicable.

As shown in Tab. 1, the shooting method yields less relative errors than the 4th-order WKB, showing that the former exhibits higher precision than the latter. Moreover, considering that the shooting method is much more efficient than the Prony method because the latter relies on complicated waveform simulations, we therefore prefer to apply the shooting method to the calculation of amplification factors in Sec. 5.

4.4.2 Data of quasi-normal modes

Our analyses reveal that the regularization parameter A_λ has a significant impact on the QNMs of massless scalar field perturbations in Tab. 1, where we present the data on how the QNMs change with

$l = 1 = m$			
A_λ	Prony method	4th-order WKB	Shooting method
0	$0.3010 - 0.0975i$	$0.3011 - 0.0973i$ (0.03%, 0.20%)	$0.3010 - 0.0973i$ (0.00%, 0.20%)
0.05	$0.3119 - 0.0998i$	$0.3119 - 0.0996i$ (0.00%, 0.20%)	$0.3118 - 0.0996i$ (0.03%, 0.20%)
0.10	$0.3242 - 0.1023i$	$0.3242 - 0.1022i$ (0.00%, 0.10%)	$0.3240 - 0.1023i$ (0.06%, 0.00%)
0.15	$0.3382 - 0.1050i$	$0.3382 - 0.1049i$ (0.00%, 0.10%)	$0.3381 - 0.1053i$ (0.03%, 0.29%)
0.20	$0.3544 - 0.1080i$	$0.3545 - 0.1077i$ (0.03%, 0.28%)	$0.3546 - 0.1082i$ (0.06%, 0.18%)
0.25	$0.3735 - 0.1114i$	$0.3738 - 0.1108i$ (0.08%, 0.54%)	$0.3738 - 0.1112i$ (0.08%, 0.18%)
0.30	$0.3964 - 0.1150i$	$0.3968 - 0.1140i$ (0.10%, 0.87%)	$0.3962 - 0.1147i$ (0.05%, 0.26%)
0.35	$0.4245 - 0.1190i$	$0.4252 - 0.1174i$ (0.16%, 1.34%)	$0.4243 - 0.1193i$ (0.05%, 0.25%)
0.40	$0.4604 - 0.1229i$	$0.4612 - 0.1207i$ (0.17%, 1.79%)	$0.4608 - 0.1227i$ (0.09%, 0.16%)
0.45	$0.5082 - 0.1256i$	$0.5093 - 0.1232i$ (0.22%, 1.91%)	$0.5079 - 0.1258i$ (0.06%, 0.16%)
$l = 2 = m$			
A_λ	Prony method	4th-order WKB	Shooting method
0	$0.4995 - 0.0967i$	$0.4995 - 0.0966i$ (0.00%, 0.10%)	$0.4994 - 0.0967i$ (0.02%, 0.00%)
0.05	$0.5179 - 0.0989i$	$0.5179 - 0.0989i$ (0.00%, 0.00%)	$0.5180 - 0.0990i$ (0.02%, 0.10%)
0.10	$0.5388 - 0.1015i$	$0.5388 - 0.1014i$ (0.00%, 0.10%)	$0.5389 - 0.1014i$ (0.02%, 0.10%)
0.15	$0.5627 - 0.1042i$	$0.5627 - 0.1042i$ (0.00%, 0.00%)	$0.5626 - 0.1042i$ (0.02%, 0.00%)
0.20	$0.5904 - 0.1073i$	$0.5904 - 0.1073i$ (0.00%, 0.00%)	$0.5903 - 0.1074i$ (0.02%, 0.09%)
0.25	$0.6231 - 0.1108i$	$0.6231 - 0.1107i$ (0.00%, 0.09%)	$0.6232 - 0.1107i$ (0.02%, 0.09%)
0.30	$0.6626 - 0.1146i$	$0.6626 - 0.1145i$ (0.00%, 0.09%)	$0.6624 - 0.1146i$ (0.03%, 0.00%)
0.35	$0.7114 - 0.1187i$	$0.7115 - 0.1185i$ (0.01%, 0.17%)	$0.7116 - 0.1187i$ (0.03%, 0.00%)
0.40	$0.7743 - 0.1229i$	$0.7743 - 0.1225i$ (0.00%, 0.32%)	$0.7743 - 0.1229i$ (0.00%, 0.00%)
0.45	$0.8588 - 0.1255i$	$0.8587 - 0.1250i$ (0.01%, 0.40%)	$0.8588 - 0.1257i$ (0.00%, 0.16%)

Table 1: QNMs for the modes of $l = 1 = m$ and $l = 2 = m$, respectively, where $a = 0.1$, $M_B = 1$, and $\mu = 0$ are set.

respect to the regularization parameter A_λ for both $l = 1 = m$ and $l = 2 = m$ modes when $a = 0.1$ and $M_B = 1$ are set. In the two modes, the real parts ω_R grow with an increase of the regularization parameter A_λ . This indicates that an increase of A_λ amplifies the oscillation frequencies of scalar fields. For example, in the mode of $l = 1 = m$, the real part corresponding to $A_\lambda = 0.45$ is 1.69 times larger than that corresponding to $A_\lambda = 0$. Furthermore, as A_λ increases, the absolute value of imaginary parts $|\omega_I|$ also increases, indicating a faster dissipation of waveforms. For instance, in the mode of $l = 1 = m$, $|\omega_I|$ corresponding to $A_\lambda = 0.45$ is 1.29 times larger than that corresponding to $A_\lambda = 0$. These results highlight the significance of regularization parameter A_λ in influencing the behaviors of QNMs of massless scalar field perturbations. Now we present the influence of A_λ on the QNMs of massless scalar field perturbations under different values of a in Fig. 3, where the maximum value of A_λ is determined by Eq. (16). Here we take the mode of $l = 1 = m$ as an example and set $M_B = 1$. As shown in Figs. 3(a) and 3(b), the real parts of QNMs always increase with an increase of A_λ under a fixed a , where the largest real part is $\omega_R = 0.7828$, located at $a = 1$ and $A_\lambda = 0.125$, and it corresponds to the extreme configuration of rLQGBHs with the greatest angular momentum, $a_{\text{Max}} = 1$. Moreover, as shown in Figs. 3(c) and 3(d),

a	$\mu = 0$			$\mu = 0.1$	
	Prony method	4th-order WKB	Shooting method	4th-order WKB	Shooting method
0	$0.3145 - 0.1024i$	$0.3146 - 0.1022i$	$0.3144 - 0.1022i$	$0.3187 - 0.0998i$	$0.3186 - 0.0996i$
0.1	$0.3242 - 0.1023i$	$0.3242 - 0.1022i$	$0.3240 - 0.1023i$	$0.3281 - 0.0999i$	$0.3278 - 0.0999i$
0.2	$0.3351 - 0.1020i$	$0.3351 - 0.1019i$	$0.3349 - 0.1022i$	$0.3388 - 0.0998i$	$0.3385 - 0.1000i$
0.3	$0.3474 - 0.1014i$	$0.3474 - 0.1012i$	$0.3475 - 0.1016i$	$0.3509 - 0.0993i$	$0.3509 - 0.0998i$
0.4	$0.3617 - 0.1004i$	$0.3617 - 0.0995i$	$0.3619 - 0.1004i$	$0.3649 - 0.0978i$	$0.3651 - 0.0989i$
0.5	$0.3785 - 0.0987i$	$0.3782 - 0.0939i$	$0.3785 - 0.0986i$	$0.3808 - 0.0923i$	$0.3816 - 0.0972i$
0.6	$0.3987 - 0.0962i$	$0.3909 - 0.0761i$	$0.3986 - 0.0961i$	$0.3924 - 0.0752i$	$0.4013 - 0.0949i$
0.7	$0.4242 - 0.0921i$	$0.3849 - 0.0530i$	$0.4242 - 0.0921i$	$0.3860 - 0.0530i$	$0.4265 - 0.0912i$
0.8	$0.4585 - 0.0850i$	$0.3693 - 0.0380i$	$0.4585 - 0.0849i$	$0.3697 - 0.0381i$	$0.4605 - 0.0843i$
0.9	$0.5116 - 0.0706i$	$0.3535 - 0.0292i$	$0.5116 - 0.0706i$	$0.3529 - 0.0292i$	$0.5129 - 0.0703i$

Table 2: QNMs for the mode of $l = 1 = m$ with $A_\lambda = 0.1$, $a = 0.1$, $M_B = 1$, $\mu = 0$ or $\mu = 0.1$. Note that the Prony method is unsuitable for massive scalar field perturbations, so no corresponding data are shown.

A_λ has diverse effects on $|\omega_1|$ under different values of a , which can be divided into three categories:

- When $0 < a \leq 0.48$, $|\omega_1|$ increases at first and then decreases when A_λ grows. Within the entire range of A_λ , $|\omega_1|$ is always larger than that corresponding to $A_\lambda = 0$. From a physical perspective, a non-vanishing A_λ gives rise to a faster decay of massless scalar fields than the case of vanishing A_λ , thereby making the spacetime more unstable. Note that an rLQGBH reaches its extreme configuration when A_λ takes its maximum value, see Eq. (16), and it reduces to a Kerr black hole when A_λ equals zero. When a increases, the gap between $|\omega_1|$ of an extreme rLQGBH and that of a Kerr black hole is getting smaller and smaller, and finally it disappears when $a = 0.48$.
- When $0.48 < a \leq 0.82$, $|\omega_1|$ also initially increases and then decreases when A_λ grows. The inflection depends on the critical value of A_λ that is associated with a . When A_λ exceeds such a value, $|\omega_1|$ is smaller than that of the Kerr case. In Fig. 3(c), we show that the critical value equals 0.38 if $a = 0.60$, and equals 0.23 if $a = 0.80$, respectively. Therefore, A_λ plays the role in promoting the stability of spacetime when A_λ is larger than this value, but it plays the role in diminishing the stability of spacetime when A_λ is smaller than this value. Additionally, this critical value becomes small when a increases, and it reaches zero when $a = 0.82$.
- When $0.82 < a \leq 1.00$, $|\omega_1|$ decreases monotonically when A_λ grows, implying that A_λ plays the role in promoting the stability of spacetime. When $a = 1$ and $A_\lambda = 0.125$, $|\omega_1|$ reaches the minimum value, $|\omega_1|_{\text{Min}} = 0.0202$.

In addition, we present the influence of A_λ on the QNMs of massless scalar field perturbations under different values of a for the mode of $l = 2 = m$ in Fig. 4, where the maximum value of A_λ is also determined by Eq. (16). In general, the influence of A_λ on QNMs in the mode of $l = 2 = m$ is similar to that in the mode of $l = 1 = m$, i.e., the former differs from the latter just in numerical differences. For the real parts of QNMs, the former is significantly larger than the latter. But for the absolute value of imaginary parts, the difference between the two modes is very small. Similarly, for the mode of $l = 2 =$

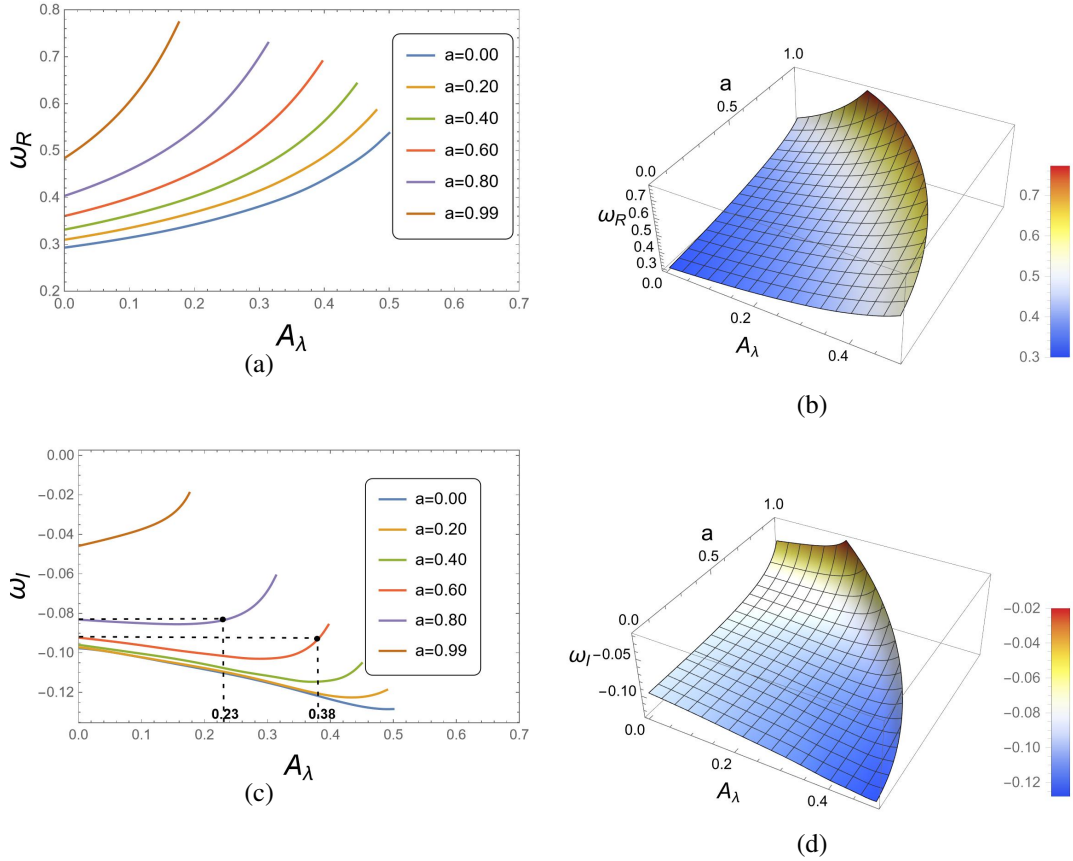


Figure 3: QNM frequencies ω as a function of regularization parameter A_λ with a varying angular momentum, $a = 0, 0.2, 0.4, 0.6, 0.8,$ and 0.99 , where $M_B = 1$ and $\mu = 0$ are set, and the mode of $l = 1 = m$ is chosen. In diagram (c), $|\omega_I|$ of rLQGBHs is smaller than that of Kerr black holes ($A_\lambda = 0$) when A_λ is greater than 0.38 for the case of $a = 0.60$, and the same phenomenon happens when A_λ is greater than 0.23 for the case of $a = 0.80$.

m , the influence of A_λ on $|\omega_I|$ can also be divided into three categories for a varying a : $0 < a \leq 0.49$, $0.49 < a \leq 0.84$, and $0.84 < a \leq 1.00$. From Fig. 4 it is clear that the relations between ω_R ($|\omega_I|$) and A_λ are quite similar in the two modes.

In Fig. 5, we demonstrate the relationship between the QNMs and regularization parameter A_λ under a varying scalar field mass μ . It can be observed for a fixed A_λ that the presence of μ leads to an increase of the real parts of ω but a decrease of the absolute value of imaginary parts. This implies that the massive scalar field perturbations around rLQGBHs oscillate faster but decay more slowly compared to the massless case, and that the mass μ plays the role in promoting the stability of spacetime. When $A_\lambda = 0$, i.e., in Kerr black holes μ has the greatest influence on the QNMs. When A_λ gradually increases, the influence of μ gradually decreases. Therefore, a non-vanishing A_λ makes μ have a weaker effect on promoting the spacetime stability than a vanishing A_λ does.

At the end of this section, we make a comment that a pure imaginary frequency means a mode that has no oscillation but just damping. In our study for rLQGBHs, we do not find any pure imaginary

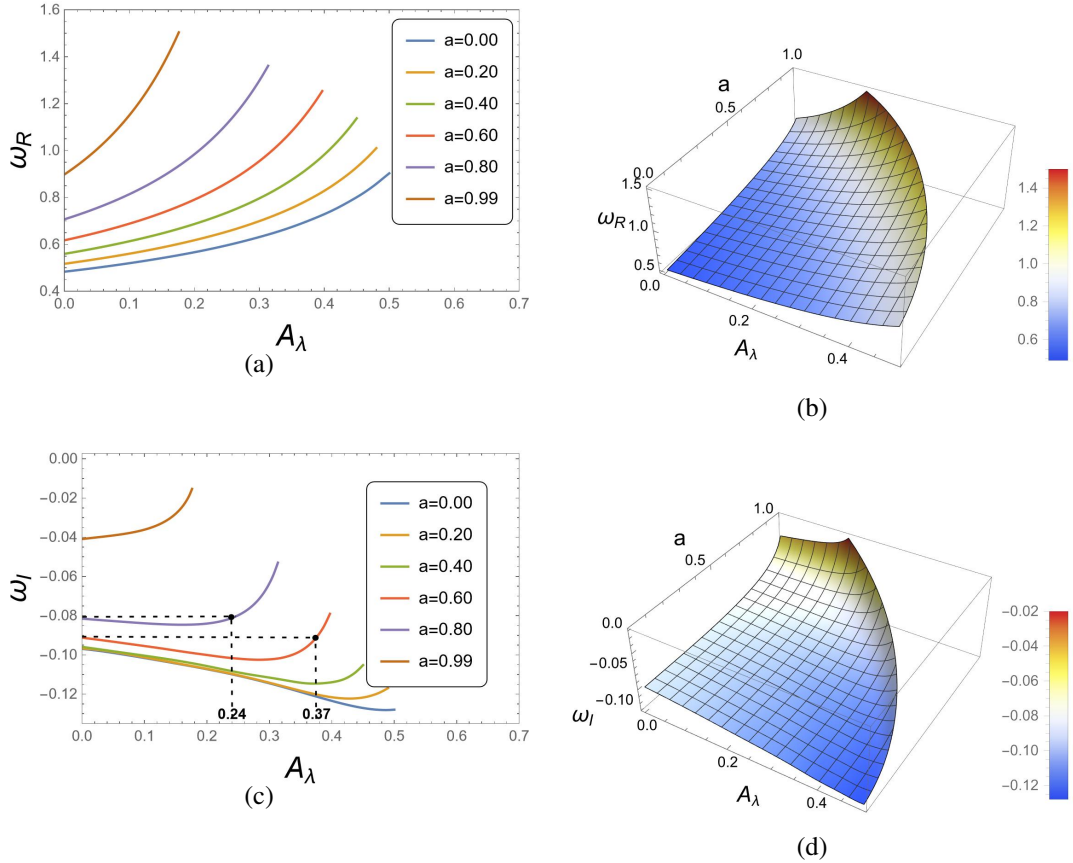


Figure 4: QNM frequencies ω as a function of regularization parameter A_λ with a varying angular momentum, $a = 0, 0.2, 0.4, 0.6, 0.8,$ and 0.99 , where $M_B = 1$ and $\mu = 0$ are set, and the mode of $l = 2 = m$ is chosen. In diagram (c), $|\omega_I|$ of rLQGBHs is smaller than that of Kerr black holes ($A_\lambda = 0$) when A_λ is greater than 0.37 for the case of $a = 0.60$, and the same phenomenon happens when A_λ is greater than 0.24 for the case of $a = 0.80$.

frequency in the damping oscillation stage. According to the results shown in Tabs. 1 and 2 together with Figs. 3, 4, and 5, it is evident that the real parts increase when A_λ and a increase, and that they can never go to zero even if A_λ and a vanish. Specifically, for $n = 0$ modes with $l = 1 = m$ and $l = 2 = m$, we can see that the real parts are non-zero for Schwarzschild black holes with vanishing A_λ and a , and that the real parts of such modes for rLQGBHs become large when A_λ and a are increasing.

5 Superradiance

The idea of extracting energy from rotating black holes was initially proposed by Penrose [43], which is based on the phenomenon of negative energy orbits within the ergosphere of black holes, now known as the Penrose process. However, the conditions to realize the Penrose process are so stringent that the process can hardly be observed in astrophysical phenomena. Inspired by the Penrose process, several more realistic mechanisms for energy extraction were subsequently suggested, including the

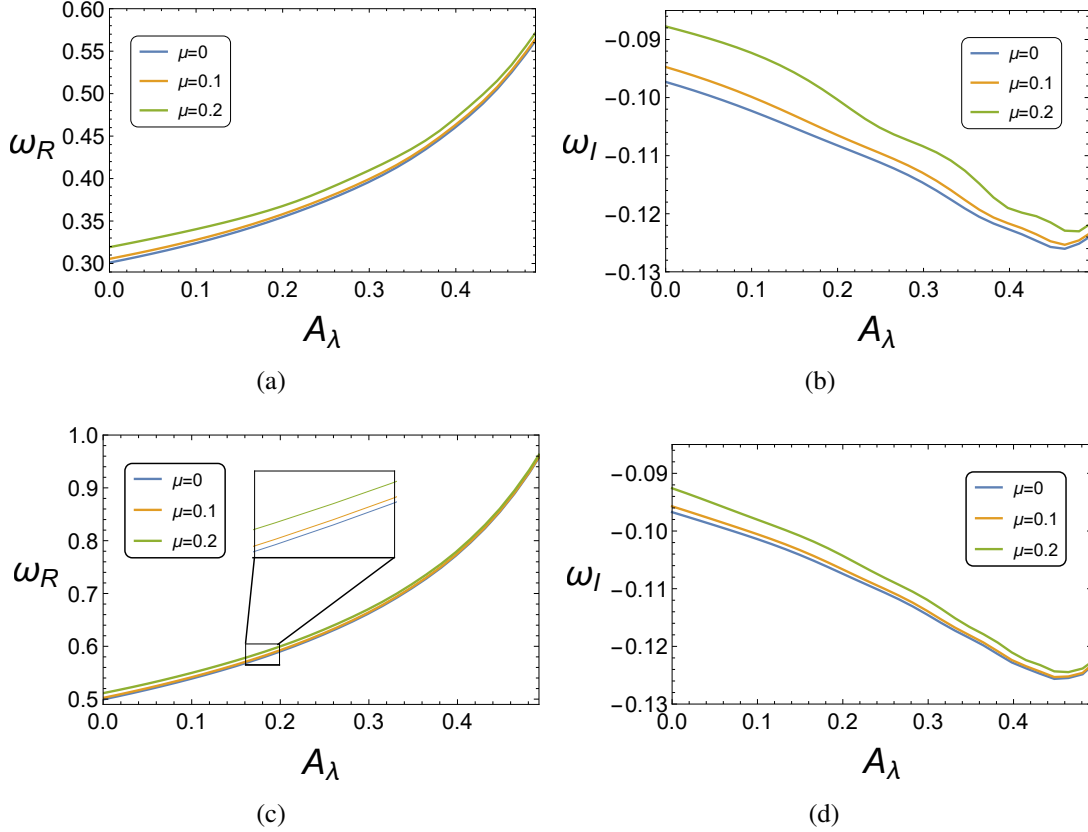


Figure 5: QNM frequencies ω as a function of regularization parameter A_λ with different masses of scalar fields, $\mu = 0, 0.1, \text{ and } 0.2$, where $a = 0.1$, $M_B = 1$, and $n = 0$ are set. The upper two diagrams correspond to the mode of $l = 1 = m$, and the lower two diagrams the mode of $l = 2 = m$.

superradiance and Blandford-Znajek mechanism [44], and so on. Among these mechanisms, the scalar superradiance recently attracts lots of attention. Unlike the Penrose process, the scalar superradiance involves ultralight scalar fields, where such scalar fields are promising candidates of dark matter. The mechanism of superradiance exploits the interaction of scalar fields with rotating black holes to amplify the fields and extract energy, providing a fascinating sample of how quantum field theory concepts might be observable in astrophysical contexts. Owing to such a close relationship between the Penrose process and superradiance, we briefly introduce this process in the next subsection.

5.1 The Penrose process

The Penrose process involves particle dynamics near a black hole, and it is closely related to the phenomenon of superradiance. Here we qualitatively infer the effects of the regularization parameter by analyzing the impact of this parameter on the Penrose process. For a particle with mass μ_0 that decays into two particles each with mass μ_f , the efficiency of energy extraction can be expressed [18, 45] as

follows:

$$\eta = \frac{1}{2} \left[\sqrt{(1 + g_{tt}) \left(1 - \frac{4\mu_f^2}{\mu_0^2} \right)} - 1 \right], \quad (52)$$

where g_{tt} means the (t, t) component of the rLQGBH metric, see Eqs. (2), (3), (6), (7), and (8). The efficiency reaches its maximum when g_{tt} takes its maximum value and the two particles are photons with vanishing mass, $\mu_f = 0$.

The metric of rLQGBHs differs from that of Kerr black holes because it incorporates an additional regularization parameter A_λ . As shown in Fig. 1 which displays the parameter space of rLQGBHs, the range of A_λ is constrained by the angular momentum a . Within the permissible parameter space, the maximal efficiency reads²

$$\eta_{\max} = \frac{1}{2} \left[\sqrt{\frac{2M_B h_0 - 6A_{\lambda 0} M_B^2}{h_0^2 - 6A_{\lambda 0} M_B^2}} - 1 \right], \quad (53)$$

where $h_0 = M_B$ and $A_{\lambda 0} = 1/8$. As a result, we obtain $\eta_{\max} \approx 0.618$, which is significantly higher than the efficiency of $\eta_{\max} \approx 0.207$ for extreme Kerr black holes.

Through the above simple analysis to the Penrose process, we find that the introduction of the regularization parameter results in a theoretically higher maximum efficiency of extractable energy from rLQGBHs compared to the Kerr scenario. Therefore, we can conclude that the energy extraction is relatively more economic from rLQGBHs than from Kerr black holes [45].

5.2 Numerical method for superradiance

When a free scalar field is incident on a black hole, the incident wave will be decomposed into two parts, a reflected wave and a transmitted wave, due to the scattering effect of potential barriers near the black hole. The boundary conditions of the scattering process include pure ingoing wave at the event horizon and both ingoing wave and outgoing wave at the spatial infinity, where the ingoing wave at the event horizon corresponds to the transmitted wave, while the ingoing wave and outgoing wave at the spatial infinity correspond to the incident wave and reflected wave, respectively. The energy of reflected waves is greater than the energy of incident waves when the frequency ω of incident scalar fields satisfies [46] the following conditions:

$$m\Omega_H > \omega > \mu, \quad (54)$$

where

$$\Omega_H = \frac{a}{h_+^2 - 6A_\lambda M_B^2 + a^2} \quad (55)$$

is the angular velocity of scalar particles at the outer event horizon h_+ determined by Eq. (15) for rLQGBHs. It is worth noting that the frequency ω of scalar fields is always real owing to the special boundary conditions of scattering processes. This phenomenon of energy amplification is called [18]

²Substituting $\mu_f = 0$ into Eq. (52) and scanning the parameter space (A_λ, a) for searching the maximum value of g_{tt} , we thus reach the maximal efficiency. For the details of the parameter space, see Sec. 2.

superradiance. Next we study how the energy amplification factor is affected by the regularization parameter A_λ .

In terms of the boundary conditions mentioned above, the radial equation of motion Eq. (38) takes the asymptotic solution at the spatial infinity as follows:

$$R(h) \sim \mathcal{I} \frac{1}{h} e^{-qh} h^{-M_B(\mu^2 - 2\omega^2)/q} + \mathcal{R} \frac{1}{h} e^{qh} h^{M_B(\mu^2 - 2\omega^2)/q}, \quad (56)$$

where \mathcal{I} and \mathcal{R} stand for the incident and reflection amplitudes, respectively. Moreover, the asymptotic wave function near the outer horizon h_+ reads

$$R(h) \sim \mathcal{T} (h - h_+)^{i\alpha}, \quad (57)$$

where \mathcal{T} is the transmission amplitude. Then the amplification factor is given [18] by

$$Z_{lm} = \frac{dE_{\text{out}}}{dE_{\text{in}}} = \left| \frac{\mathcal{R}}{\mathcal{I}} \right|^2 - 1. \quad (58)$$

Following the shooting method outlined in Sec. 4.3, we establish the relationship among \mathcal{I} , \mathcal{R} , and \mathcal{T} , and thus give the amplification factor of superradiance.

5.3 Results

In Fig. 6 we present the relations between the amplification factor and ω under a varying A_λ for a massless incident particle and a massive one with mass $\mu = 0.2$, respectively. In the region where the superradiance effect appears, the energy amplification factor always increases at first and then decreases as the particle frequency ω grows. On the boundaries of the region, $\omega = \mu$ and $\omega = m\Omega_H$, see Eq. (54) with $M_B = 1$, the amplification factor is always zero. Moreover, the amplification factor decreases as the particle mass μ increases, indicating that the superradiance effect is inhibited by particle mass.

The influence of regularization parameter A_λ on the amplification factor varies with the particle frequency ω . When the particle frequency ω is low, a small A_λ leads to an amplification factor that is larger than that led by a big A_λ . The specific situation can be observed in the small picture of Fig. 6(a), where an increase of A_λ restrains the superradiance effect in the region of small ω . However, as ω gradually increases, the amplification factor associated with a small A_λ is gradually surpassed by the amplification factor associated with a big A_λ . Ultimately, a larger A_λ results in a greater peak of amplification factors. On the whole, an increase of A_λ plays the role in promoting the superradiance effect.

6 Conclusion

In the present work, we investigate the scalar field perturbations in the background of rLQGBHs. By employing the hyperbolic foliation equation, as expressed in Eq. (24), we successfully navigate numerical challenges at the boundaries, enabling us to accurately characterize the time-domain evolution profiles of scalar fields around rLQGBHs. Interestingly, we observe that while A_λ does not significantly

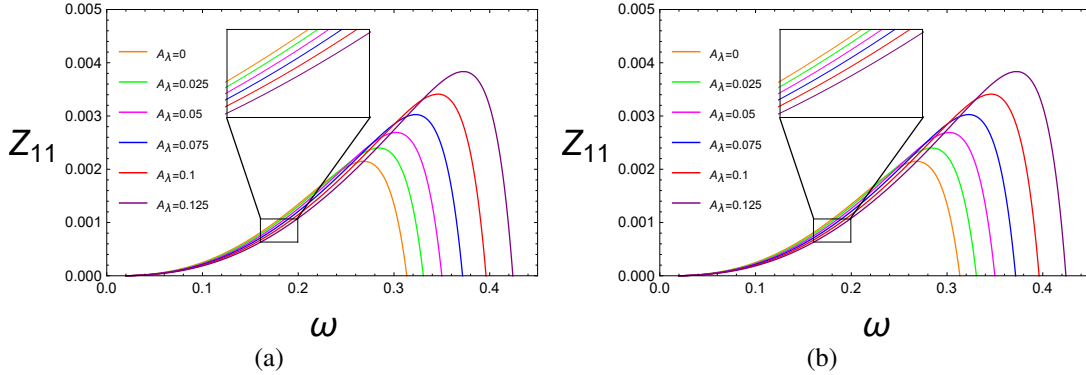


Figure 6: Amplification factor with respect to the frequency of scalar fields for the mode of $l = 1 = m$ in rLQGBHs, where $n = 0$, $M_{\text{B}} = 1$, and $a = 0.9$ are set. The left diagram corresponds to the case of massless scalar fields, $\mu = 0$, and the right one to the case of massive scalar fields with mass $\mu = 0.2$.

impact the outburst and late-time tail stages of scalar field evolution, it markedly influences the damping oscillation stage. To further elucidate the effect of A_{λ} on the scalar field evolution, we employ the Prony method, the fourth-order WKB method, and the shooting method to extract QNMs from the damping oscillations. Among these methods, the Prony method emerges as the most precise, while the shooting method is highlighted for its numerical efficiency.

Our exploration reveals that the influence of the scalar field mass μ on the QNMs is alleviated with an increase of A_{λ} . Moreover, we investigate how A_{λ} influences the QNMs by taking different values of angular momentum a , uncovering that the effect of A_{λ} on the QNMs varies with the angular momentum. This underscores the significant role played by the regularization parameter in affecting the QNMs of rLQGBHs.

Furthermore, we examine the impact of A_{λ} on the superradiance effect in the background of rLQGBHs, finding that A_{λ} not only broadens the frequency range susceptible to superradiance but also significantly enhances the efficiency of superradiant amplification, particularly when $\omega \sim m\Omega_{\text{H}}$.

Based on our comprehensive investigation of QNMs and superradiance, we conclude that the regularization parameter A_{λ} is pivotal in shaping the dynamics of ultralight massive scalar fields in the background of rLQGBHs. Our findings provide novel insights into the behavior of rLQGBHs and set the stage for future inquiries into the dynamical behaviors of rotating LQG wormholes, addressing the challenges posed by their unique boundary conditions. As we chart the course for future research, our work not only enriches the theoretical landscape of black hole physics but also opens new avenues for exploration within the quantum gravity domain.

Acknowledgments

Y-GM would like to thank Emmanuele Battista, Stefan Fredenhagen, and Harold Steinacker for the warm hospitality during his stay at University of Vienna. We would also like to thank Shao-Jun Zhang for his suggestions in the calculation of waveforms. This work was supported in part by the National

References

- [1] S. W. Hawking. Black hole explosions. *Nature*, 248:30–31, 1974. doi:10.1038/248030a0.
- [2] Roger Penrose. Gravitational collapse: The role of general relativity. *Nuovo Cimento Rivista Serie*, 1:252, 1969. doi:10.1103/PhysRevLett.14.57.
- [3] Chen Lan, Hao Yang, Yang Guo, and Yan-Gang Miao. Regular Black Holes: A Short Topic Review. *Int. J. Theor. Phys.*, 62(9):202, 2023. arXiv:2303.11696, doi:10.1007/s10773-023-05454-1.
- [4] James Bardeen. Non-singular general relativistic gravitational collapse. In *Proceedings of the 5th International Conference on Gravitation and the Theory of Relativity*, page 87, 1968.
- [5] Alfio Bonanno and Martin Reuter. Renormalization group improved black hole space-times. *Phys. Rev. D*, 62:043008, 2000. arXiv:hep-th/0002196, doi:10.1103/PhysRevD.62.043008.
- [6] Benjamin Koch and Frank Saueressig. Black holes within Asymptotic Safety. *Int. J. Mod. Phys. A*, 29(8):1430011, 2014. arXiv:1401.4452, doi:10.1142/S0217751X14300117.
- [7] Mariam Bouhmadi-López, Che-Yu Chen, Xiao Yan Chew, Yen Chin Ong, and Dong-Han Yeom. Regular Black Hole Interior Spacetime Supported by Three-Form Field. *Eur. Phys. J. C*, 81(4):278, 2021. arXiv:2005.13260, doi:10.1140/epjc/s10052-021-09080-1.
- [8] Leonardo Modesto. Loop quantum black hole. *Class. Quant. Grav.*, 23:5587–5602, 2006. arXiv:gr-qc/0509078, doi:10.1088/0264-9381/23/18/006.
- [9] Rodolfo Gambini and Jorge Pullin. Loop quantization of the Schwarzschild black hole. *Phys. Rev. Lett.*, 110(21):211301, 2013. arXiv:1302.5265, doi:10.1103/PhysRevLett.110.211301.
- [10] Norbert Bodendorfer, Fabio M. Mele, and Johannes Münch. (b,v)-type variables for black to white hole transitions in effective loop quantum gravity. *Phys. Lett. B*, 819:136390, 2021. arXiv:1911.12646, doi:10.1016/j.physletb.2021.136390.
- [11] Norbert Bodendorfer, Fabio M. Mele, and Johannes Münch. Mass and Horizon Dirac Observables in Effective Models of Quantum Black-to-White Hole Transition. *Class. Quant. Grav.*, 38(9):095002, 2021. arXiv:1912.00774, doi:10.1088/1361-6382/abe05d.
- [12] Suddhasattwa Brahma, Che-Yu Chen, and Dong-han Yeom. Testing Loop Quantum Gravity from Observational Consequences of Nonsingular Rotating Black Holes. *Phys. Rev.*

- Lett.*, 126(18):181301, 2021. arXiv:2012.08785, doi:10.1103/PhysRevLett.126.181301.
- [13] Misba Afrin, Sunny Vagnozzi, and Sushant G. Ghosh. Tests of Loop Quantum Gravity from the Event Horizon Telescope Results of Sgr A*. *Astrophys. J.*, 944(2):149, 2023. arXiv:2209.12584, doi:10.3847/1538-4357/acb334.
- [14] R. A. Konoplya and A. Zhidenko. Quasinormal modes of black holes: From astrophysics to string theory. *Rev. Mod. Phys.*, 83:793–836, 2011. arXiv:1102.4014, doi:10.1103/RevModPhys.83.793.
- [15] K. D. Kokkotas and B. G. Schmidt. Quasi-normal modes of stars and black holes. *Living Reviews in Relativity*, 2(1):2, 1999. arXiv:gr-qc/9909058, doi:10.12942/lrr-1999-2.
- [16] Zhen Li. Scalar perturbation around rotating regular black hole: Superradiance instability and quasinormal modes. *Phys. Rev. D*, 107(4):044013, 2023. arXiv:2210.14062, doi:10.1103/PhysRevD.107.044013.
- [17] Edgardo Franzin, Stefano Liberati, Jacopo Mazza, Ramit Dey, and Sumanta Chakraborty. Scalar perturbations around rotating regular black holes and wormholes: Quasinormal modes, ergoregion instability, and superradiance. *Phys. Rev. D*, 105(12):124051, 2022. arXiv:2201.01650, doi:10.1103/PhysRevD.105.124051.
- [18] Richard Brito, Vitor Cardoso, and Paolo Pani. Superradiance: New Frontiers in Black Hole Physics. *Lect. Notes Phys.*, 906:pp.1–237, 2015. arXiv:1501.06570, doi:10.1007/978-3-319-19000-6.
- [19] Vitor Cardoso, Seth Hopper, Caio FB Macedo, Carlos Palenzuela, and Paolo Pani. Gravitational-wave signatures of exotic compact objects and of quantum corrections at the horizon scale. *Physical Review D*, 94(8):084031, 2016. URL: <https://doi.org/10.1103/PhysRevD.94.084031>, arXiv:1608.08637, doi:10.1103/PhysRevD.94.084031.
- [20] Davide Gerosa and Maya Fishbach. Hierarchical mergers of stellar-mass black holes and their gravitational-wave signatures. *Nature Astronomy*, 5(8):749–760, 2021. doi:10.1038/s41550-021-01398-w.
- [21] Lukas R. Weih, Matthias Hanauske, and Luciano Rezzolla. Postmerger Gravitational-Wave Signatures of Phase Transitions in Binary Mergers. *Phys. Rev. Lett.*, 124(17):171103, 2020. arXiv:1912.09340, doi:10.1103/PhysRevLett.124.171103.
- [22] W. H. Press and S. A. Teukolsky. Floating orbits, superradiant scattering and the black-hole bomb. *Nature*, 238(5362):211–212, 1972. doi:10.1038/238211a0.
- [23] J. D. Bekenstein. Extraction of energy and charge from a black hole. *Physical Review D*, 7(8):949–953, 1973. doi:10.1103/PhysRevD.7.949.

- [24] Y. B. Zeldovich. Amplification of cylindrical electromagnetic waves reflected from a rotating body. *Soviet Journal of Experimental and Theoretical Physics Letters*, 14(3):180–181, 1971.
- [25] A. A. Starobinsky and S. M. Churilov. Amplification of electromagnetic and gravitational waves scattered by a rotating "black hole". *Soviet Physics JETP*, 38(1):1–5, 1973.
- [26] William E. East. Massive Boson Superradiant Instability of Black Holes: Nonlinear Growth, Saturation, and Gravitational Radiation. *Phys. Rev. Lett.*, 121(13):131104, 2018. arXiv:1807.00043, doi:10.1103/PhysRevLett.121.131104.
- [27] Edward W Leaver. An analytic representation for the quasi-normal modes of kerr black holes. *Proceedings of the Royal Society of London. A. Mathematical and Physical Sciences*, 402(1823):285–298, 1985. doi:10.1098/rspa.1985.0119.
- [28] Edward W Leaver. Quasinormal modes of reissner-nordström black holes. *Physical Review D*, 41(10):2986, 1990. doi:10.1103/PhysRevD.41.2986.
- [29] Mustapha Azreg-Aïnou. Generating rotating regular black hole solutions without complexification. *Phys. Rev. D*, 90(6):064041, 2014. arXiv:1405.2569, doi:10.1103/PhysRevD.90.064041.
- [30] Ingrid Thuestad, Gaurav Khanna, and Richard H. Price. Scalar fields in black hole spacetimes. *Physical Review D*, 96(2):024020, 2017. arXiv:arXiv:1704.05096, doi:10.1103/PhysRevD.96.024020.
- [31] Shao-Jun Zhang, Bin Wang, Anzhong Wang, and Joel F Saavedra. Object picture of scalar field perturbation on kerr black hole in scalar-einstein-gauss-bonnet theory. *Physical Review D*, 102(12):124056, 2020. arXiv:2007.10348, doi:10.1103/PhysRevD.102.124056.
- [32] Enno Harms, Sebastiano Bernuzzi, Alessandro Nagar, and An Zenginoglu. A new gravitational wave generation algorithm for particle perturbations of the Kerr spacetime. *Class. Quant. Grav.*, 31(24):245004, 2014. arXiv:1406.5983, doi:10.1088/0264-9381/31/24/245004.
- [33] William E Schiesser. *The numerical method of lines: integration of partial differential equations*. Elsevier, 2012.
- [34] Yang Guo, Hao Xie, and Yan-Gang Miao. Signal of phase transition hidden in quasinormal modes of regular AdS black holes. *Phys. Lett. B*, 855:138801, 2024. arXiv:2402.10406, doi:10.1016/j.physletb.2024.138801.
- [35] Emanuele Berti, Vitor Cardoso, Jose A. Gonzalez, and Ulrich Sperhake. Mining information from binary black hole mergers: A Comparison of estimation methods for complex exponentials in noise. *Phys. Rev. D*, 75:124017, 2007. arXiv:gr-qc/0701086, doi:10.1103/PhysRevD.75.124017.

- [36] S. Chandrasekhar and Steven L. Detweiler. The quasi-normal modes of the Schwarzschild black hole. *Proc. Roy. Soc. Lond. A*, 344:441–452, 1975. doi:10.1098/rspa.1975.0112.
- [37] C. Molina, Paolo Pani, Vitor Cardoso, and Leonardo Gualtieri. Gravitational signature of Schwarzschild black holes in dynamical Chern-Simons gravity. *Phys. Rev. D*, 81:124021, 2010. arXiv:1004.4007, doi:10.1103/PhysRevD.81.124021.
- [38] Sai Iyer. BLACK HOLE NORMAL MODES: A WKB APPROACH. 2. SCHWARZSCHILD BLACK HOLES. *Phys. Rev. D*, 35:3632, 1987. doi:10.1103/PhysRevD.35.3632.
- [39] Edward Seidel and Sai Iyer. BLACK HOLE NORMAL MODES: A WKB APPROACH. 4. KERR BLACK HOLES. *Phys. Rev. D*, 41:374–382, 1990. doi:10.1103/PhysRevD.41.374.
- [40] R. A. Konoplya, A. Zhidenko, and A. F. Zinhailo. Higher order WKB formula for quasinormal modes and grey-body factors: recipes for quick and accurate calculations. *Class. Quant. Grav.*, 36:155002, 2019. arXiv:1904.10333, doi:10.1088/1361-6382/ab2e25.
- [41] R. A. Konoplya. Quasinormal behavior of the d-dimensional Schwarzschild black hole and higher order WKB approach. *Phys. Rev. D*, 68:024018, 2003. arXiv:gr-qc/0303052, doi:10.1103/PhysRevD.68.024018.
- [42] RA Konoplya and AV Zhidenko. Stability and quasinormal modes of the massive scalar field around kerr black holes. *Physical Review D*, 73(12):124040, 2006. arXiv:gr-qc/0605013, doi:10.1103/PhysRevD.73.124040.
- [43] Roger Penrose and RM Floyd. Extraction of rotational energy from a black hole. *Nature Physical Science*, 229(6):177–179, 1971.
- [44] Serguei S Komissarov. Blandford-znajek mechanism versus penrose process. 2008. arXiv:0804.1912.
- [45] Subrahmanyan Chandrasekhar. *The mathematical theory of black holes*, volume 69. Oxford university press, 1998.
- [46] Si-Jiang Yang, Yu-Peng Zhang, Shao-Wen Wei, and Yu-Xiao Liu. Destroying the event horizon of a nonsingular rotating quantum-corrected black hole. *JHEP*, 04:066, 2022. arXiv:2201.03381, doi:10.1007/JHEP04(2022)066.